

See discussions, stats, and author profiles for this publication at: <https://www.researchgate.net/publication/282732793>

# Ion Dynamics in Solid Electrolytes: NMR Reveals the Elementary Steps of Li<sup>+</sup> Hopping in the Garnet Li<sub>6.5</sub>La<sub>3</sub>Zr<sub>1.75</sub>Mo<sub>0.25</sub>O<sub>12</sub>

ARTICLE in CHEMISTRY OF MATERIALS · SEPTEMBER 2015

Impact Factor: 8.35 · DOI: 10.1021/acs.chemmater.5b02231

CITATION

1

READS

30

5 AUTHORS, INCLUDING:



**Daniel Rettenwander**

University of Salzburg

15 PUBLICATIONS 53 CITATIONS

SEE PROFILE



**Walter Schmidt**

Graz University of Technology

3 PUBLICATIONS 10 CITATIONS

SEE PROFILE



**Georg Amthauer**

University of Salzburg

172 PUBLICATIONS 1,742 CITATIONS

SEE PROFILE



**Martin Wilkening**

Graz University of Technology

119 PUBLICATIONS 1,564 CITATIONS

SEE PROFILE

# Ion Dynamics in Solid Electrolytes: NMR Reveals the Elementary Steps of Li<sup>+</sup> Hopping in the Garnet Li<sub>6.5</sub>La<sub>3</sub>Zr<sub>1.75</sub>Mo<sub>0.25</sub>O<sub>12</sub>

Patrick Bottke,<sup>\*,†,‡</sup> Daniel Rettenwander,<sup>¶</sup> Walter Schmidt,<sup>†</sup> Georg Amthauer,<sup>¶</sup> and Martin Wilkening<sup>\*,†,‡</sup>

<sup>†</sup>Christian Doppler Laboratory for Lithium Batteries, Institute for Chemistry and Technology of Materials, Graz University of Technology (NAWI Graz), 8010 Graz, Austria

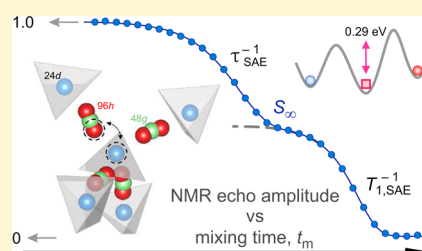
<sup>‡</sup>DFG Research Unit 1277 'molife', Graz University of Technology, 8010 Graz, Austria

<sup>¶</sup>Department of Materials Research and Physics, University of Salzburg, 5020 Salzburg, Austria

## S Supporting Information

**ABSTRACT:** Garnet-type oxides are considered to belong to the most attractive solid Li<sup>+</sup> electrolytes. This is due to their wide electrochemical stability window as well as their superior ionic conductivity, with a Li-ion transference number of almost one. Usually ionic conductivities are studied via impedance spectroscopy on a macroscopic length scale. Time-domain NMR methods, however, have been used much less extensively to shed light on the elementary hopping processes in highly conducting oxide garnets. Here, we used NMR relaxometry and stimulated echo NMR to study Li<sup>+</sup> self-diffusion in Li<sub>6.5</sub>La<sub>3</sub>Zr<sub>1.75</sub>Mo<sub>0.25</sub>O<sub>12</sub> (LLZMO), which served as a model compound to collect information on the <sup>7</sup>Li spin dynamics. It turned out

that NMR spin–lattice relaxation (SLR) recorded in both the laboratory and rotating frame of reference shows features that seem to be a universal fingerprint for fast conducting garnets that have been stabilized in their cubic modification. In contrast to Al-doped garnet-type Li<sub>7</sub>La<sub>3</sub>Zr<sub>2</sub>O<sub>12</sub> that modifies the Li sublattice, in LLZMO the Li sublattice remains intact, offering the possibility to get to the bottom of Li-ion dynamics in LLZO-based garnets. Most importantly, whereas NMR SLR rates measured at 194.3 MHz reflect an almost universal behavior of local hoppings being thermally activated by only 0.151(3) eV, the spin-lock technique (33.3 kHz) gives evidence of two separate, overlapping rate peaks with activation energies on the order of 0.29 eV for the elementary steps of Li-ion hopping. This points to a less pronounced distribution of Li<sup>+</sup> jump rates on the kilohertz time scale than has been observed for the Al-stabilized LLZO samples. The NMR results obtained also entail information on both the Li<sup>+</sup> diffusion coefficients and the shape of the underlying motional correlation functions. The latter has been provided by <sup>7</sup>Li NMR spin-alignment echo correlation spectroscopy that also shows the involvement of 24d and 96h sites in Li<sup>+</sup> diffusion.



## 1. INTRODUCTION

Clean energy storage is one of the most urgent issues that has to be solved if we are to stop our dependency on fossil fuels. There is general agreement about the need to cut CO<sub>2</sub> emissions by storing electricity generated from renewable sources via, e.g., powerful and sustainable systems that store energy electrochemically.<sup>1–5</sup>

Ionically conducting solid electrolytes<sup>6–8</sup> are key to developing advanced all-solid-state batteries based on Li<sup>+</sup> as ionic charge carriers. In order to replace flammable liquid electrolytes, which are commonly used in lithium-ion batteries, Li-bearing sulfides and oxides are being feverishly searched to identify those that fulfill the requirements placed on solid electrolytes.<sup>7–18</sup> Considering oxides, garnet-type electrolytes are currently in the spotlight of materials science and battery research.<sup>7,19</sup>

In 2007, Murugan et al. reported on a very high Li-ion conductivity (10<sup>−3</sup> to 10<sup>−4</sup> S cm<sup>−1</sup>) in garnet-type Li<sub>7</sub>La<sub>3</sub>Zr<sub>2</sub>O<sub>12</sub> (LLZO) crystallizing with cubic symmetry (space group *Ia* $\bar{3}$ d).<sup>9</sup> Since then, many papers have been published focusing on both synthesis and characterization of ion transport in Li-bearing garnets; an overview is given by Thangadurai and co-workers.<sup>19</sup> The electrochemical stability of LLZO has been studied

recently by the Sakamoto group.<sup>20</sup> Nowadays, we know that aliovalent doping of LLZO with, e.g., Al, Ga, or even Fe,<sup>21–26</sup> is essential not only to stabilize the cubic modification<sup>21,27,28</sup> against the tetragonal one<sup>29</sup> with its lower conductivity but also to free the lithium ions from their fixed sites, enabling them to quickly diffuse along various pathways in the complex oxide network.<sup>19,21</sup>

While ionic transport properties in garnets are commonly studied by impedance spectroscopy,<sup>19,30</sup> some of us reported on a comprehensive time-domain nuclear magnetic resonance (NMR) study on Al-doped LLZO in 2011.<sup>21</sup> NMR relaxometry was used to corroborate the findings from impedance spectroscopy; moreover, it was helpful to deliver further insights on Li<sup>+</sup> self-diffusion from a microscopic point of view by taking advantage of methods that are sensitive to ion hopping on the Ångström scale.<sup>21,31</sup> Such information is crucial if we are to understand the extraordinary dynamic properties of garnets. Until now, however, NMR relaxometry has been used only rarely to characterize doped Li-containing garnets.<sup>21,31,32</sup>

Received: June 2, 2015

Revised: September 11, 2015

In our preceding work,<sup>21</sup> we discovered some NMR anomalies that are anticipated to be tightly linked with the high Li-ion diffusivity probed. For example, via spin-locking  $^7\text{Li}$  NMR spin–lattice relaxation (SLR) rate measurements, an extremely broad diffusion-induced rate peak was observed,<sup>21</sup> pointing to high-temperature activation energies (ca. 0.34 eV) comparable with those from conductivity measurements. Unexpectedly, the shape of the corresponding peak in the lab frame turned out to be much different. Its so-called low- $T$  flank followed Arrhenius behavior over a large temperature range characterized by an activation energy of only 0.12 eV.

The present study is aimed at answering the question of whether this is a special feature of Al-doped LLZO or a universal one of fast Li-ion conducting garnets with cubic structure. Here,  $\text{Li}_{6.5}\text{La}_3\text{Zr}_{1.75}\text{Mo}_{0.25}\text{O}_{12}$  (LLZMO) turned out to be a promising model system to shed light on this aspect. Most importantly, as compared to Al (or Ga)-doped LLZO,<sup>21,25</sup> for which the dopants on 24d sites might act as blocking ions for  $\text{Li}^+$  transport, the cubic modification studied here is not stabilized by manipulating the Li sublattice; *au contraire*, in LLZMO the La–Zr sublattice is modified, leaving the Li sublattice untouched with respect to foreign dopants occupying the Li sites. In our opinion, this can be used to explain the differences found here when compared to the previous NMR relaxation studies on Al-doped LLZO.<sup>21</sup>

Moreover, compared to the available investigations on LLZO in the literature, in the present study we go one step further and apply spin-alignment echo (SAE) NMR correlation spectroscopy<sup>33–40</sup> to probe slow ion dynamics at temperatures well below ambient.  $^7\text{Li}$  SAE NMR is able to provide more precise information on the nature of Li-ion dynamics since it directly measures a single-spin two-time hopping correlation function;<sup>33,38,41–44</sup> it takes advantage of the quadrupolar interaction of the Li spin with electric field gradients at the nuclear sites. From temperature-variable echo decay curves, both Li activation energies, i.e., hopping barriers, and correlation times can be deduced.<sup>39,45–48</sup> In addition, SAE NMR contains information on the shape of the underlying average motional correlation function that governs fast ion transport in LLZMO.

## 2. EXPERIMENTAL SECTION

Synthesis of  $\text{Li}_{6.5}\text{La}_3\text{Zr}_{1.75}\text{Mo}_{0.25}\text{O}_{12}$  was performed by high-temperature sintering methods according to Wagner et al.<sup>49</sup> The starting materials were  $\text{Li}_2\text{CO}_3$  (99%, Merck),  $\text{La}_2\text{O}_3$  (99.99%, Aldrich),  $\text{ZrO}_2$  (99.0%, Aldrich), and  $\text{MoO}_3$  (99.98%, Aldrich).  $\text{Li}_2\text{CO}_3$  (with an excess of 10 wt % to compensate the loss of  $\text{Li}_2\text{O}$  during sintering) was mixed with the various oxides in the necessary proportions; they were ground intimately together using a hand mortar, a pestle, and isopropanol. This mixture was pressed uniaxially to a pellet and afterward calcined at 1123 K for 4 h with a heating rate of 5  $\text{K min}^{-1}$ . The pellets were put in an alumina crucible. To avoid contamination with Al from the crucible, the samples were placed on a pellet of pure LLZO. The mixture was allowed to cool in the furnace to approximately 473 K. Then, the sample was milled in isopropanol using planetary ball mill (Fritsch Pulverisette 7) for 2 h (12 times 550 rpm for 5 min with a break of 5 min between each milling period). Finally, the powder was isostatically pressed (15 kbar) to yield pellets. Afterward, the pellets were sintered at 1500 K for 4 h sandwiched between pellets of pure LLZO to avoid Li-loss during sintering; the heating rate was 20.5  $\text{K min}^{-1}$ ; after the sintering period, the pellets were allowed to cool to room temperature. The phase purity was checked via X-ray powder diffraction, neutron diffraction (Table S1), and back scattered electrons as well as energy dispersive spectroscopy using a polished pellet: no phases other than LLZMO and no elements other than Li, La, Zr, Mo, O were observed.<sup>49</sup> Finally, the Li content

was measured by means of ICP-OES, verifying the stoichiometry  $\text{Li}_{6.5}\text{La}_3\text{Zr}_{1.75}\text{Mo}_{0.25}\text{O}_{12}$ . The sample investigated crystallizes with cubic symmetry, space group  $1a\bar{3}d$ , see above.

A piece of the cylindrical pellet prepared was placed directly inside the NMR probe. A flow of dry nitrogen gas in combination with a heater inside the probe head was used to adjust the temperature inside the sample chamber. A preceding recuperator inserted in a dewar filled with liquid nitrogen was used to cool the sample below ambient conditions. We used an Avance 500 spectrometer (Bruker BioSpin) equipped with a shimmed magnet with a magnetic field  $B_0$  of 11.7 T. The  $^7\text{Li}$  resonance frequency  $\omega_0/2\pi$  to record  $^7\text{Li}$  NMR line shapes and SLR rates as a function of temperature was 194.3 kHz. While spectra under nonrotating conditions were recorded with a single  $90^\circ$  pulse, the SLR rates ( $R_1, R_{1\rho}$ ) were acquired either with the saturation recovery pulse sequence<sup>50,51</sup> or the spin-lock technique<sup>13,51–58</sup> that takes advantage of transversal relaxation along a locked  $B_1$  field. For the latter, a locking frequency of  $\gamma_m B_1 = \omega_1/2\pi = 33.3$  kHz was used; here,  $\gamma_m$  denotes the magnetogyric ratio of  $^7\text{Li}$ .

Additionally, spin–spin relaxation rates  $R_2$  and Jeener–Broekaert<sup>59</sup> echo decay rates<sup>33,36</sup> were measured. We used a two-pulse quadrupole echo pulse sequence optimized for spin  $3/2$  nuclei<sup>41</sup> to record transversal echo damping. Jeener–Broekaert echoes were generated with a  $45^\circ$  pulse following a  $90^\circ$  pulse after a short preparation time  $t_p$  of 10  $\mu\text{s}$ .<sup>33,34,37</sup> The damping of the spin-alignment (quadrupolar) echo was monitored as a function of mixing time  $t_m$ . A  $45^\circ$  reading pulse was used to transfer magnetization back into an observable signal. Optimized phase cycling<sup>41</sup> served to suppress unwanted coherence pathways; in general, a short preparation time<sup>33,34,37</sup> is necessary to eliminate dipolar contributions as effectively as possible (see below).

## 3. RESULTS AND DISCUSSION

**3.1. Change of NMR Line Shapes.** The garnet-type oxides studied by  $^7\text{Li}$  NMR spectroscopy so far are characterized by a significant line narrowing that starts at temperatures much below room temperature. The same feature is seen for the present garnet,  $\text{Li}_{6.5}\text{La}_3\text{Zr}_{1.75}\text{Mo}_{0.25}\text{O}_{12}$ . In Figure 1, selected  $^7\text{Li}$  NMR lines are shown; while Figure 1a focuses on the central transition, in Figure 1b, the satellite transitions are shown. Since  $^7\text{Li}$  is a spin  $3/2$  nucleus, the corresponding NMR line is composed of a central line ( $+1/2 \rightleftharpoons -1/2$ ) and satellite intensities that reflect the spin-transitions  $+3/2 \rightleftharpoons -3/2$ . The

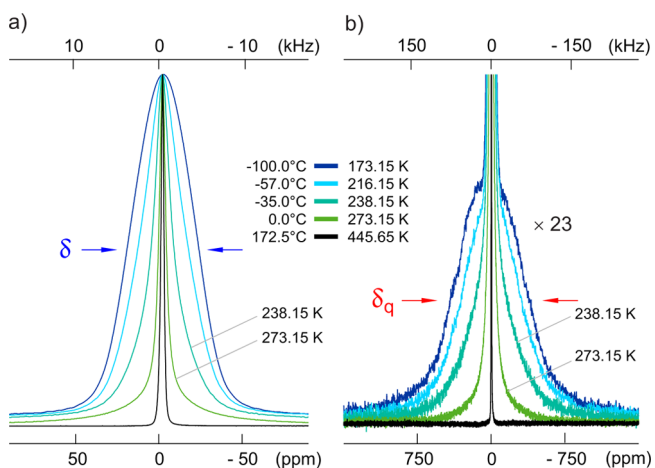


**Figure 1.** (a)  $^7\text{Li}$  NMR spectra of garnet-type, Mo-bearing  $\text{Li}_{6.5}\text{La}_3\text{Zr}_{1.75}\text{Mo}_{0.25}\text{O}_{12}$  recorded at 194.3 MHz at the temperatures indicated. The heights of the spectra are normalized; in (a), only the central line is shown. (b) Same spectra as in (a) but plotted with a magnification factor (23 times) to make the complete quadrupolar powder pattern visible.

latter interaction is of electric quadrupolar nature; it is due to the interaction of the quadrupole moment of  $^7\text{Li}$  with nonvanishing electric field gradients (EFGs) in the direct neighborhood of the nucleus.<sup>60</sup> This interaction alters the Zeeman levels, giving rise, in the case of a single crystal, to a central line flanked by two satellite transitions. For powder samples, on the other hand, the orientation dependence of the electric quadrupole interactions results in a broad quadrupolar powder pattern.<sup>60</sup> The more electrically inequivalent sites Li occupies, i.e., the more EFGs are present, the more complex the resulting overall line shape at low temperature will be. At sufficiently low  $T$ , where ion dynamics do not affect the line shape, called the *rigid lattice* regime, the quadrupole intensities can usually be approximated with a Gaussian function. Similarly, in this  $T$  regime, the central line, which reflects the magnetic dipolar interactions, shows, in many cases, a Gaussian shape.

With increasing mobility of the Li spins, however, magnetic dipolar as well as electric quadrupolar interactions are continuously averaged. This manifests itself in pronounced line narrowing,<sup>61</sup> which is shown in Figure 1a. While at 173.15 K the line recorded is as expected for the rigid lattice regime, ion dynamics start to affect the line widths already at 183.15 K. Above 273 K, the line is almost fully narrowed, indicating very fast Li-ion hopping processes. The  $^7\text{Li}$  NMR line widths (fwhm, (overall) full width at half-maximum) are shown in Figure 2 as

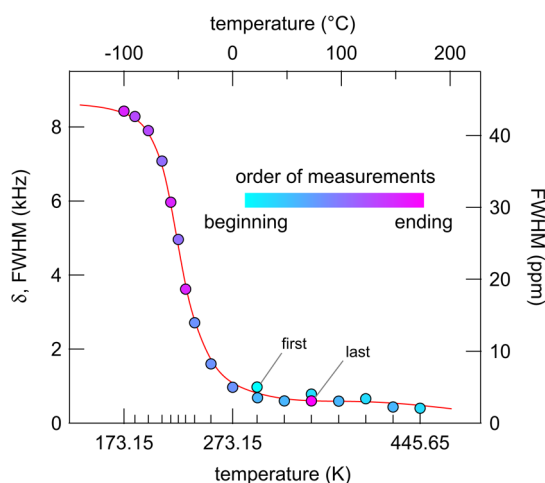


**Figure 2.** (a) The  $^7\text{Li}$  NMR line width of the central transition (fwhm, full width at half-maximum) of  $\text{Li}_{6.5}\text{La}_3\text{Zr}_{1.75}\text{Mo}_{0.25}\text{O}_{12}$  as a function of temperature. The color of the data points refer to the measuring order of the lines. It turned out that the powder sample, which was measured as a piece of the pellet in dry  $\text{N}_2$  atmosphere, is stable over the whole  $T$  range investigated.

a function of temperature. Starting with a rigid lattice line width,  $\delta_0$ , of ca. 9 kHz, the line reaches half of its initial value at ca. 240 K. At the inflection point of the motional narrowing curve, the  $\text{Li}^+$  jump rate  $\tau^{-1}$  is approximately given by  $\tau^{-1} = \delta_0 \times 2\pi \approx 5.6 \times 10^4 \text{ s}^{-1}$ . At room temperature, which is the normal operation temperature for solid-state batteries,  $\tau^{-1}$  is expected to be much larger (see below).

Interestingly, the  $^7\text{Li}$  NMR line shapes, in contrast to what has been observed for Al-doped LLZO, undergo a relatively homogeneous motional narrowing. This means that almost the whole line is affected by the narrowing process; for Al-doped LLZO, we found a marked heterogeneous motional narrowing

that points to mobile ions next to less mobile ions in the garnet structure. Here, the smooth transition from a Gaussian shape toward a Lorentzian line at elevated  $T$  indicates that the majority of Li ions take part in the diffusion process even at relatively low  $T$ . This is a noteworthy difference compared to Li-bearing garnets stabilized by aliovalent Al doping.

Line narrowing is sensitive to ion dynamics determined by the spectral width of the NMR component under investigation. While  $\delta_0$  is on the order of 9 kHz, the quadrupole intensities (see Figure 1b) span a spectral range of ca. 300 kHz. The width of the quadrupole foot,  $\delta_q$ , is ca. 150 kHz. This is 10 times larger than  $\delta_0$ . Hence, full averaging of the quadrupole intensities is expected if the jump rate reaches values (significantly) larger than  $\delta_q$ . While at 273.15 K the satellite intensity has drastically lost in intensity, it has completely been vanished at 445.65 K. Already at 395.65 K the mean jump rate has increased to values much larger than  $10^6 \text{ s}^{-1}$  at least. The fact that averaging of quadrupole satellites sets in at relatively low temperatures and that it accompanies narrowing of the central line, which is sensitive to slower Li-ion diffusion, points to a subensemble of Li ions that are quite mobile on the time scale set by  $\delta_q$ . This feature shows that we cannot interpret the data with the help of a single diffusion process only. Our  $^7\text{Li}$  NMR SLR measurements, see next section, clearly underpin this view.

**3.2. Diffusion-Induced NMR Spin–Lattice Relaxation Rates.** To quantify Li-ion diffusion parameters in crystalline  $\text{Li}_{6.5}\text{La}_3\text{Zr}_{1.75}\text{Mo}_{0.25}\text{O}_{12}$ , we recorded both  $^7\text{Li}$  NMR SLR rates ( $T_1^{-1}$ ) in (i) the laboratory frame of reference ( $\omega_0/2\pi = 194.3 \text{ MHz}$ ) and (ii) in the so-called rotating frame of reference<sup>56–58</sup> ( $T_{1\rho}^{-1}$ ) by utilizing an angular spin-lock frequency  $\omega_0/2\pi$  that is much lower than the Larmor frequency  $\omega_0/2\pi$  (Figure 3). Hence, spin-lock NMR is sensitive to slower Li-ion dynamics as compared to that of  $T_1^{-1}$  NMR experiments.<sup>39,40,62</sup>

At first, we will present the  $T_1^{-1}$  results. The corresponding transients, which describe the recovery of longitudinal magnetization  $M_z$  as a function of delay time  $t_d$ , can be best parametrized with single exponentials:  $M_z(t_d) \propto 1 - \exp(-t/T_1)$ , where  $\gamma_1$  deviates only slightly from 1. The rates  $T_1^{-1}$  and the corresponding stretching exponents  $\gamma_1$  are shown in the Arrhenius plot of Figure 3. At low temperatures,  $T_1^{-1}$  deviates from Arrhenius behavior due to nondiffusive effects on  $M_z(t_d)$ . These can be lattice vibrations and coupling of the  $^7\text{Li}$  spins to paramagnetic centers.<sup>63</sup> Above 250 K, the rates  $T_1^{-1}$  follow an Arrhenius law that is given by  $T_1^{-1} \propto \exp(-E_a/k_B T)$ .  $k_B$  denotes Boltzmann's constant, and  $E_a$  is the activation energy. Here, we found  $E_a = 0.151(3) \text{ eV}$ . Although it is slightly larger, this value is comparable with previous results on Al-doped garnets (0.12 eV).<sup>21</sup> Since  $E_a$  is smaller than the activation energy that is commonly found by conductivity spectroscopy, which is sensitive to long-range ion transport, the recovery of  $M_z(t_d)$  is likely induced by short-range motions of the Li ions. These may also include unsuccessful, i.e., forward–backward, Li jumps that are accompanied by correlation effects.<sup>64–66</sup> The value of 0.151(3) eV might be closely related to the activation energy that represents the barrier of an elementary  $\text{Li}^+$  jump process in LLZMO.

On the basis of the present result, the rather shallow increase of  $T_1^{-1}$  seems to be a universal feature of the highly conducting garnets with cubic symmetry investigated by NMR so far. This is in stark contrast to what is seen for the tetragonal modification of LLZO, whose ion conductivity is lower by 2 orders of magnitude.<sup>29,31</sup> For tetragonal LLZO, which does not



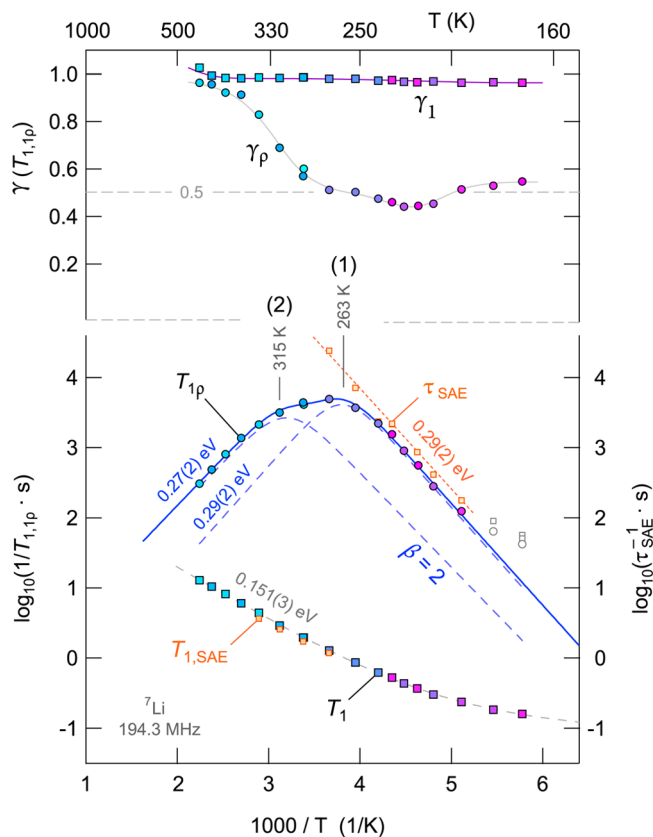


**Figure 3.** Arrhenius plot of the  $^7\text{Li}$  SLR NMR rates  $T_1^{-1}$  and  $T_{1q}^{-1}$  of crystalline  $\text{Li}_{6.5}\text{La}_3\text{Zr}_{1.75}\text{Mo}_{0.25}\text{O}_{12}$ . The Larmor frequency was 194.3 MHz, and we used a locking frequency of  $\omega_1/2\pi$  of 33.3 kHz to record the  $M_\rho(t_{\text{lock}})$  transients that are shown in Figure 4. The continuous line represents the sum of two single rate peaks that are characterized by the dashed lines shown. The dashed line drawn through the  $T_1^{-1}$  data points is a combination of an Arrhenius fit with a power-law fit that takes into account background relaxation at low  $T$ . The solid lines in the upper part of the graph, which show the temperature dependence of  $\gamma_1$  and  $\gamma_p$ , are just to guide the eye. For comparison, decay rates obtained from SAE NMR are also shown. The dotted line is an Arrhenius fit yielding 0.29 eV; the corresponding rates  $T_{1,\text{SAE}}^{-1}$ , which coincide with  $T_1^{-1}$ , are also included.

need stabilization via Al doping, the rates  $T_1^{-1}$  follow a low- $T$  flank of a diffusion-induced rate peak that is characterized by 0.32 eV.<sup>31</sup> The same low- $T$  activation energy was found by  $T_{1q}^{-1}$ . Altogether, a joint fit of  $T_{1q}^{-1}(1/T)$  and  $T_1^{-1}(1/T)$  resulted in 0.48 eV.<sup>31</sup> This value is directly comparable with activation energies deduced from conductivity spectroscopy (0.47 eV).

By formally replacing  $\omega_0$  by  $\omega_1$ , we are able to shift the low- $T$  SLR rate flank toward lower temperatures.<sup>39</sup> This enables us to record the complete diffusion-induced rate peak  $T_{1q}^{-1}(1/T)$ , as has been shown for tetragonal LLZO and Al-doped, cubic LLZO.<sup>21,31</sup> In general, the peak maximum shows up at  $\omega_{0(1)}\tau_c \approx 1$ , where the correlation time  $\tau_c$  is identical with the jump rate  $\tau$  within a factor of 2.<sup>51</sup> The corresponding rates  $T_{1q}^{-1}$  are included in Figure 3. They have been extracted from transversal magnetization transients  $M_\rho(t_{\text{lock}})$  by varying the spin-lock time  $t_{\text{lock}}$  from 10  $\mu\text{s}$  up to 0.5 s. The transients obtained are presented in Figure 4. Solid lines show fits with stretched exponentials according to  $M_\rho(t_{\text{lock}}) \propto 1 - \exp(-(t/T_{1p})^{\gamma_p})$ . The stretching factor  $\gamma_p$  strongly varies with temperature. It takes values of ca. 0.5 at low temperatures, where  $\omega_1\tau \gg 1$  holds. Such a  $\sqrt{(t_{\text{lock}})}$  decay behavior is expected for  $T_{1q}$  transients

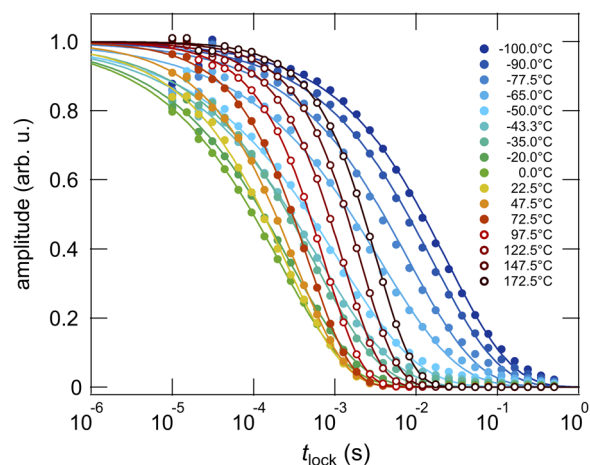


**Figure 4.**  $^7\text{Li}$  NMR  $T_{1q}$  transients,  $M_\rho$  amplitude vs locking time normalized to range between 0 and 1, that were recorded with the spin-lock technique. The solid lines represent fits according to  $M_\rho(t_{\text{lock}}) \propto \exp(-(t/T_{1p})^{\gamma_p})$ . The stretching exponents obtained,  $\gamma_p$ , are shown in Figure 3. At the highest temperatures,  $M_\rho(t_{\text{lock}})$  follows a single exponential.

that are governed by interactions of the Li spins with paramagnetic impurities.<sup>67</sup> At high temperatures, i.e., in the regime  $\omega_1\tau \ll 1$ , the exponent  $\gamma_p$  strives toward  $\gamma_p = 1$ , which is reached at approximately 450 K. The increase of  $\gamma_p$  shows up when  $T_{1q}^{-1}$  has passed through the peak maximum, i.e., when reaching the limit  $\omega_1\tau \ll 1$ . It is likely that in this  $T$  range the shape of the underlying (averaged) motional correlation function resembles that of a pure exponential.

At first glance, the shape of the rate peak  $T_{1q}^{-1}(1/T)$  turns out to be rather broad. In the present case, however, it is much narrower than what has been observed for Al-doped (and Ga-doped) LLZO. For LLZO, this has been interpreted as a large distribution of jump rates and activation energies that leads to a superposition of many SLR rate peaks showing up at different temperatures. In the present case, instead, the shape of  $T_{1q}^{-1}(1/T)$  can be well-reproduced with a combination of only two individual rate peaks. The two peaks are shown in Figure 3 as dashed lines.

We used the SLR NMR model according to BPP theory that relies on a Lorentzian shaped spectral density function  $J(\omega_{0(1)})$  to which the rate  $T_{1(1q)}^{-1}$  is proportional to<sup>60</sup>

$$J(\alpha\omega_{0(1)})_{\alpha=1,2} = C_{0(1)}\tau_c/(1 + (\alpha\omega_{0(1)}\tau_c)^\beta) \quad (1)$$

The data  $T_{1q}^{-1}(1/T)$  can be approximated with the following expression for 3D motion

$$T_{1q}^{-1} = C_q \left( J(2\omega_1) + \frac{5}{3}J(\omega_0) + \frac{2}{3}J(2\omega_0) \right) \quad (2)$$

The parameter  $\beta$  in eq 1 reflects deviations from the case of uncorrelated motion.  $\tau_c$  is given by  $\tau_c \approx \tau = \tau_0^{-1} \exp(-E_{aq}/(k_B T))$ . Here, the best fits were obtained with  $\beta = 2$ , i.e., a simple BPP-type spectral density function is sufficient to reproduce the rate peaks.  $\beta = 2$  leads to symmetric rate peaks.

Interestingly, the shape of the two peaks is rather similar. In the limit  $\omega_1\tau \gg 1$ , we obtain  $E_{aq}^{\text{low}} \approx 0.29$  eV; almost the same value governs the rates in the regime  $\omega_1\tau \gg 1$ , for which  $E_{aq}$  is given by 0.29(2) eV (peak 1) and 0.27(2) eV (peak 2). The latter value, which refers to the peak at lower  $T$ , is definitely smaller than the activation energy of tetragonal LLZO (0.42

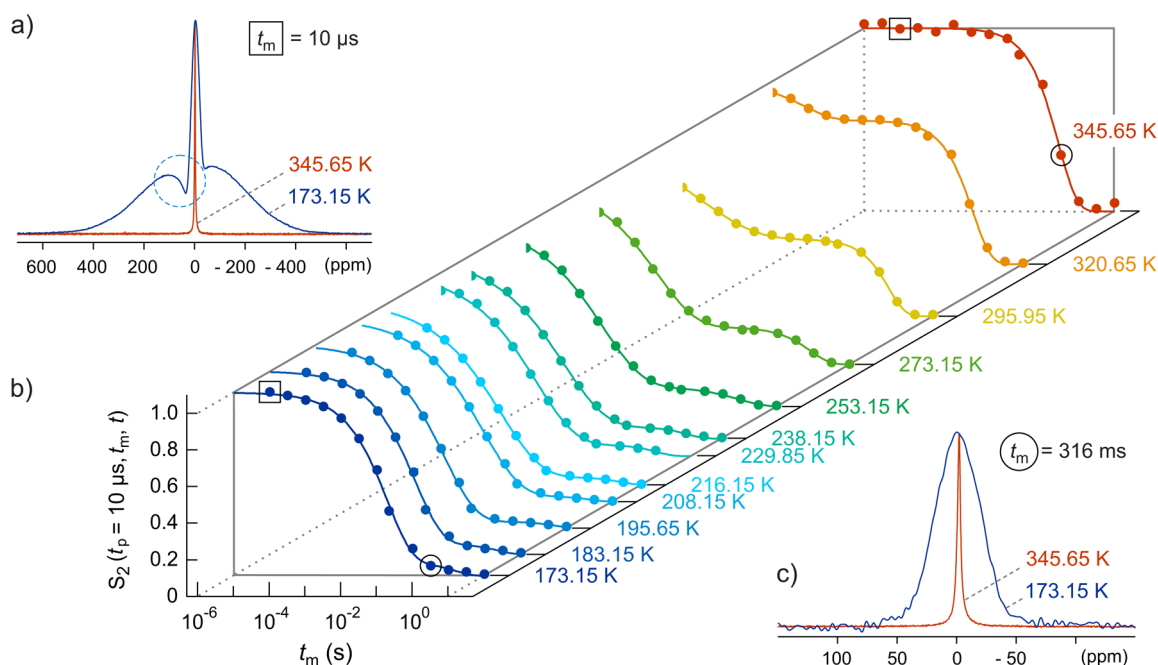


**Figure 5.** (a) Fourier transforms (173.15 and 345.65 K) of the  $^{7}\text{Li}$  spin-alignment echoes of  $\text{Li}_{6.5}\text{La}_3\text{Zr}_{1.75}\text{Mo}_{0.25}\text{O}_{12}$  that were recorded at  $t_p = 10\ \mu\text{s}$  and short  $t_m = 10\ \mu\text{s}$ , i.e., before ion dynamics has an effect on the echo amplitude; in (c), the Fourier transforms at  $t_m = 316\ \text{ms}$  are shown for comparison. (b) Stacked plot of the  $^{7}\text{Li}$  NMR SAE single-spin (sin–sin) two-time correlation functions recorded at  $t_p = 10\ \mu\text{s}$ . From ca. 200 K to ca. 273 K, the first decay step is visible that contains the rate  $\tau_{\text{SAE}}^{-1}$ , which can be identified with the  $\text{Li}^+$  jump rate  $\tau^{-1}$ . At 345.65 K, echo damping is governed solely by spin–lattice relaxation characterized by  $T_{1,\text{SAE}}^{-1}$ ; the two rates are shown in Figure 3. See text for further details.

eV). This suggests high overall  $\text{Li}^+$  diffusivity. The fact that peak 1 shows up at lower  $T$  is due to the larger prefactor obtained. Here, we have  $\tau_0^{-1}(1) = 1.6 \times 10^{11}\ \text{s}^{-1}$  and a rather small value for  $\tau_0^{-1}(2)$ , viz.,  $8 \times 10^9\ \text{s}^{-1}$ .

Considering the fitting results, it is obviously possible to probe two different, quite fast, diffusion processes in LLZMO. Note that in the present case such information is neither available by  $T_1$  nor by line shape measurements; it is seen solely in  $T_{1Q}^{-1}(1/T)$ . The separation into two peaks enables us to determine the temperatures of the peak maxima and to estimate  $\text{Li}^+$  self-diffusion coefficients. Here, the rate peaks  $T_{1Q}^{-1}(1/T)$  show up at  $T_{\text{max},1} = 263\ \text{K}$  and  $T_{\text{max},2} = 315\ \text{K}$ . With  $\omega_0\tau \approx 0.5$ , which is valid for  $T_{1Q}$  at the peak maximum, the jump rate  $\tau^{-1}(T_{\text{max}})$  is given by  $4.2 \times 10^5\ \text{s}^{-1}$ . Using the Einstein–Smoluchowski equation,  $D = a^2/(6\tau)$ , this yields a self-diffusion coefficient  $D$  of ca.  $1.9 \times 10^{-11}\ \text{cm}^2\ \text{s}^{-1}$  at 263 K (and 313 K, respectively). Here, we choose the jump distance  $a$  to be equal to the distance between the  $\text{Li}^+$  sites 24d and 96h ( $a = 1.66\ \text{\AA}$ , see below).

**3.3. Li Jumps in LLZMO as Seen via Stimulated Echo NMR.** In order to find out whether the activation energy of 0.29 eV can also be seen by other NMR techniques, we employed stimulated echo correlation spectroscopy. In detail, we used the Jeener–Broekaert three-pulse sequence<sup>59</sup> to record (sinus–sinus) two-time single-spin correlation functions<sup>38</sup> (see Figures 5 and 6).

**3.3.1. SAE Decay Curves Recorded at Short Preparation Times.** By using a short preparation time  $t_p$  of  $10\ \mu\text{s}$  between the first and second pulses, a spin state close to that of ideal spin-alignment can be reached, as has been shown by Wu and co-workers.<sup>33</sup> The corresponding spin-alignment echo (SAE) that is recorded after a variable mixing time  $t_m$  ( $10\ \mu\text{s} \leq t_m \leq 10\ \text{s}$ ) shows up after the reading pulse. Its amplitude,  $S_2(t_p = \text{const.}, t_m, t = t_p)$ , decays either (i) due to slow  $\text{Li}^+$  jump

processes between sites with different EFGs, i.e.,  $\tau_{\text{SAE}}^{-1} \approx \tau^{-1}$ , (ii) because of ordinary (quadrupolar) NMR spin–lattice relaxation ( $T_{1,\text{SAE}}^{-1}$ ), or (iii) because of spin-diffusion effects ( $T_{1,\text{sd}}^{-1}$ ):<sup>43,44</sup>

$$S_2 \propto \exp[-(t_m/\tau_{\text{SAE}})^\gamma] \cdot A \quad (3)$$

with

$$A = \exp[-(t_m/T_{1,Q})^{\gamma'}] \exp[-(t_m/T_{1,\text{sd}})^{\gamma''}]$$

The pure SAE decay is given by  $S_2' \propto \exp[-(t_m/\tau_{\text{SAE}})^\gamma]$ . In many cases, the  $\text{Li}^+$  jump process proceeds on a shorter time scale than the latter two effects; hence, it is possible to separate the term  $S_2' \propto \exp[-(t_m/\tau_{\text{SAE}})^\gamma]$  from the nondiffusive ones. Indeed, this is the case here; as we will present below, a two-step decay shows up that can be attributed to  $S_2'$  and to the term  $\exp[-(t_m/T_{1,Q})^{\gamma'}]$ , where, in our case,  $T_{1,Q}$  equals  $T_1$ .<sup>44,48</sup>

Another way of separation can be chosen if SAE curves have been recorded down to sufficiently low  $T$ . At low  $T$ , the damping is mainly governed by  $T_{1,Q}$  or  $T_{1,\text{sd}}$ ; this helps to estimate the influence of the two rates on the echo decay of interest.<sup>43</sup> Additional help is given by the fact that  $T_{1,\text{sd}}^{-1}$  is expected to change only little with temperature. This is, however, in contrast to  $\tau_{\text{SAE}}^{-1}$ , which, in the ideal case, resembles the temperature dependence of ionic conductivities, as has been shown for quite a large number of examples.<sup>39,45–47,68,69</sup> Hence, via SAE NMR, it is possible to access long-range (bulk) ion transport parameters with the help of a microscopic tool.<sup>39</sup> Moreover, in certain cases, it provides information on the geometry, that is, the diffusion pathways of  $\text{Li}$  ions.<sup>40,63</sup>

The  $^{7}\text{Li}$  SAE NMR curves recorded for the oxide garnet  $\text{Li}_{6.5}\text{La}_3\text{Zr}_{1.75}\text{Mo}_{0.25}\text{O}_{12}$  are shown in Figure 5. At the lowest temperatures, a one-step echo decay is seen; the SAE curve obtained can be parametrized with a stretched exponential function. With increasing temperature, the curves shift toward shorter mixing times, indicating that  $\text{Li}$  jumps between

electrically inequivalent sites and increasingly causing echo damping. Simultaneously, at long mixing times, a second decay process gains in intensity. While the first process is leaving the accessible time window, the latter process dominates the  $S_2$  curves at elevated  $T$ . This is also illustrated in Figure 6; for

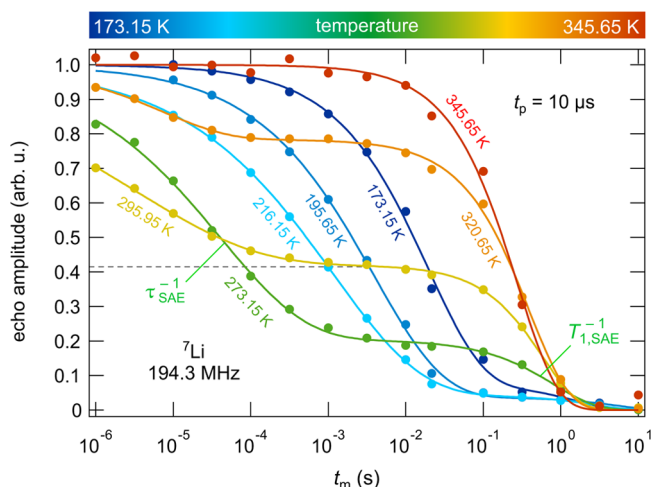


**Figure 6.**  $^7\text{Li}$  SAE NMR two-time correlation functions  $S_2(t_p = \text{const.}, t_m, t = t_p)$  recorded at  $t_p = 10 \mu\text{s}$ . The amplitude of the quadrupolar spin-alignment echo is plotted vs mixing time  $t_m$ . Data have been recorded at 194.3 MHz. The solid lines show fits being a sum of two exponential functions that contain the rates  $\tau_{\text{SAE}}^{-1}$  and  $T_{1,\text{SAE}}^{-1}$ ; the two-step decay feature is at best seen at 273.15 K. The emergence of the second decay step can have different origins; see text for further explanation.

example, the curve recorded at 273.15 K reveals the two-step decay behavior best. Note that for those recorded above 300 K the normalization turned out to be difficult; thus, arbitrary scaling is used for the data recorded at 320.65 and 345.65 K.

Analyzing the temperature dependence of the SAE NMR rates (see the Arrhenius plot in Figure 3) clearly reveals their origins. At the highest temperatures, the rates of the second decay step coincide with  $T_1^{-1}$ :  $T_{1,\text{Q}}^{-1} = T_1^{-1}$ . The rates of the first decay step, however, follow Arrhenius behavior down to ca. 200 K. Below this temperature, they deviate from Arrhenius behavior. It is most likely that spin-diffusion affects echo decay at low  $T$ . The fit shown in Figure 3, which does not take into account the last two data points, yields an activation energy,  $E_{\text{a,SAE}}$  of 0.29 eV. This value is consistent with that deduced from SLR NMR in the rotating frame of reference ( $E_{\text{a,Q}}$ ); see above. Moreover, it also agrees with that obtained from preliminary impedance spectroscopy measurements (ca. 0.3 eV) performed on the same sample.<sup>49</sup> In summary, the time-domain NMR methods applied tell us that at low temperatures (<300 K) bulk long-range lithium-ion transport in LLZMO is characterized by an activation energy of approximately 0.30 eV. This activation energy is slightly smaller than that found for Al-doped LLZO (0.34 eV).<sup>21</sup>

Coming back to the two-step decay behavior of our  $S_2$  curves that evolves with increasing temperature, we have to ask the following question: what we can learn about the underlying spin system? As expected, the first decay step shifts toward shorter mixing times the faster the Li-ions jump between the available nonequivalent  $\text{Li}^+$  sites in LLZMO. We should keep in mind that only a limited number of crystallographic sites are regularly occupied in our LLZMO sample: the tetrahedral site

24d and the split-atom site 96h; see below. Because of this circumstance, we have to consider, of course, the effect of final state amplitudes on echo decay, as will be discussed below. In addition, we have to consider the important effect of motional phase averaging as we deal with an ion conductor showing rapid Li diffusion at ambient temperature. As we can infer from the  $^7\text{Li}$  NMR spectra shown in Figure 1b, the quadrupole interactions are indeed significantly averaged due to sufficiently fast Li exchange. This process sets in at relatively low temperatures. If some or all of the Li spins “sense” a single, averaged EFG, then no temporal fluctuations of the associated quadrupole frequency is given any longer during the time period  $t_m$ . This means at the same time, the Li ions have visited a number of sites during  $t_p$  if  $\tau \lesssim t_p$ , i.e., the evolution times is not short as compared to the hopping correlation time (as discussed below).<sup>42</sup> Sensing an averaged EFG or hopping directly between electrically inequivalent sites means that the prerequisite that makes SAE NMR work gets lost; consequently, there would be no SAE decay because the rate  $\tau_{\text{SAE}}^{-1} \approx \tau^{-1}$  would be given by  $\tau_{\text{SAE}}^{-1} \rightarrow 0$  (being equivalent to  $\tau_{\text{SAE}} \rightarrow \infty$ ). Instead, the only reason for the decay of an echo formed would be because of (ordinary) spin–lattice relaxation.

Considering temperatures below ambient, we observe that the amplitude of the second step grows. This could be interpreted as follows: the spin system consists of two spin reservoirs, viz., a subsystem with slow Li spins for which SAE NMR works and a second one made up of very fast ions that already see an averaged EFG. The higher the temperature, the more ions convert into the fast reservoir. Consequently, the amplitude of the second decay step should steadily increase with temperature. For example, at 295.15 K, about 40% of the ions (Figure 6) would have access to a fast diffusion process that is invisible for SAE NMR. At 320.65 K and above, a reliable normalization of the  $S_2$  curves is no longer possible. This is because the initial amplitude of the SAE echo lies out of the accessible time window if we use short preparation times to record the data.

Considering the shape of the first decay step, there are indeed indications of heterogeneous dynamics, although the  $^7\text{Li}$  NMR spectra do not point to pronounced heterogeneous motional narrowing. For instance, only stretched exponentials are suitable to parametrize the first decay step; see, e.g., the curve recorded at 216.15 K (Figure 6). Between 200 and 280 K, a stretching exponent  $\gamma$  (see eq 3) of 0.4 is best suited to describe echo damping of  $S_2'$ . Obviously, heterogeneous dynamics is seen only if we use the site-specific electric quadrupolar information to identify the ions rather than to rely on homonuclear dipole–dipole interactions only. Of course, the distribution width of jump rates in LLZMO is assumed to be much narrower than that of Al-doped LLZO studied previously.<sup>21</sup> Compared to Al-stabilized  $\text{Li}_7\text{La}_3\text{Zr}_2\text{O}_{12}$  in the case of LLZMO, no additional disorder on the Li sublattice is introduced. As noted above, in LLZMO the Mo ions share common sites with Zr residing on the Wyckoff position 16a; they do not directly influence the sites of the Li sublattice (24d, 96h).<sup>49</sup>

**3.3.2. SAE Decay Curves Recorded at Long Preparation Times.** Alternatively, one might think about another scenario that could explain the two-step  $S_2$  decay: While at low  $T$  the Li ions could be exchanged over various inequivalent sites, at higher temperatures a diffusion pathway connecting only electrically equivalent sites may play the dominant role. For instance, this could include direct jumps between 96h sites bypassing the 24d



site, as illustrated below. Xu et al.,<sup>70</sup> however, pointed out that such a diffusion pathway is characterized by a much higher activation energy (>0.8 eV) than that found by rotating-frame SLR NMR here.

Thus, it seems more likely that echo damping is indeed affected by heterogeneous dynamics causing (partial) phase averaging. The plateau value reached at intermediate mixing times can also be interpreted as a so-called final state amplitude,  $S_\infty$ . This means that if only a limited number of electrically inequivalent sites participate in Li diffusion then the loss of phase coherence is restricted. This would lead to a final amplitude  $S_\infty$  larger than 0. If  $S_2$  is properly normalized to range between 0 and 1, then it is given by the inverse number  $1/N$  of the quadrupole frequencies  $\omega_Q$  involved, provided the available Li sites are equally populated. If equal population is not given, then  $S_\infty$  is calculated by the summation over the squared weighing factors  $w_i$ :  $S_\infty = \sum_{i=1}^N w_i^2$ .<sup>38</sup> Considering a powder average ( $\langle \dots \rangle$ ), the pure SAE NMR decay is<sup>38,43,44</sup>

$$S'_2(t_m) \propto \langle (\sin[\omega_Q(0)t_p] \sin[\omega_Q(t_m)t_p]) \rangle \quad (4)$$

$$\propto \exp[-(t_m/\tau_{\text{SAE}})^\gamma] \quad (3')$$

relating the phase angles given by  $\omega_Q(0)t_p$  and  $\omega_Q(t_m)t_p$  (or their mean values  $\overline{\omega_Q}$ ). The final value of  $S_\infty(t_p \rightarrow \infty)$  is reached only at sufficiently large  $t_p$ ; at shorter  $t_p$ , it will vary around the final value. In general,  $S_2$  will be of the form of

$$S_2(t_m) = (A \cdot S'_2 + B) \cdot \exp[-(t_m/T_{1,Q})^{\gamma'}] \quad (5)$$

provided we consider temperatures where  $T_{1,\text{SAE}}$  equals  $T_{1,Q}$  i.e., the two-step decay regime. The final state amplitude is then given by  $S_\infty = B/(A + B)$ . Thus, to determine  $S_\infty$ , echoes at large  $t_p$  have to be recorded. For  $^7\text{Li}$ , however, this will simultaneously create (unwanted) dipolar order. This disadvantage is less important in  $^2\text{H}$  SAE NMR because of the much larger quadrupole interaction in deuteron NMR, but it is important in  $^7\text{Li}$  NMR. Therefore, SAE decay curves, and echoes as well, recorded at preparation times significantly larger than, e.g., 10  $\mu\text{s}$  will be affected by dipole–dipole interactions. Such interactions also play a role at  $t_p = 10 \mu\text{s}$  if we consider the Fourier transforms shown in Figure 5a. The apparent “central” line that shows up at low  $T$  and short  $t_p$  and  $t_m$  reflects dipolar coupling of the Li spins.<sup>41</sup> Note that at short  $t_m$  the influence of ion dynamics on echo formation is kept as low as possible. For comparison, the Fourier transforms of the second decay step (see Figure 5c) is composed of a single line that no longer contains the quadrupole intensities. In short, before we can discuss any results for  $S_\infty$ , we have to know the influence that large  $t_p$  values have on the  $S'_2(t_m)$  decay.

If  $t_p$  is increased, i.e., if  $t_p$  is (much) larger or equal to  $\tau_{\text{SAE}}$ , then phase averaging during  $t_p$  might affect echo damping. This would shift the  $S'_2(t_m)$  curve back toward longer mixing times, and, indeed, this is found here (see Figure 7). In contrast, as expected, the term  $\exp[-(t_m/T_{1,\text{SAE}})^{\gamma'}]$  is not influenced by  $t_p$ , and the increase in preparation time affects  $\tau_{\text{SAE}}^{-1}$  since  $\tau_{\text{SAE}} \gg t_p$  is no longer valid. The higher the temperature, the larger the effect because  $\tau_{\text{SAE}}$  decreases with  $T$ . In the ideal case, during a short  $t_p$ , no  $\text{Li}^+$  exchange occurs, guaranteeing the storage of all of the necessary phase information on the spins. Here, below 240 K, overall Li exchange is slow and an increase of  $t_p$  has little effect on  $\tau_{\text{SAE}}^{-1}$  (and on the amplitude  $S_\infty$ ), ensuring that the rate is useful to derive a reliable activation energy; see Figure 3. At 273 K and above, the effect of motional phase averaging during

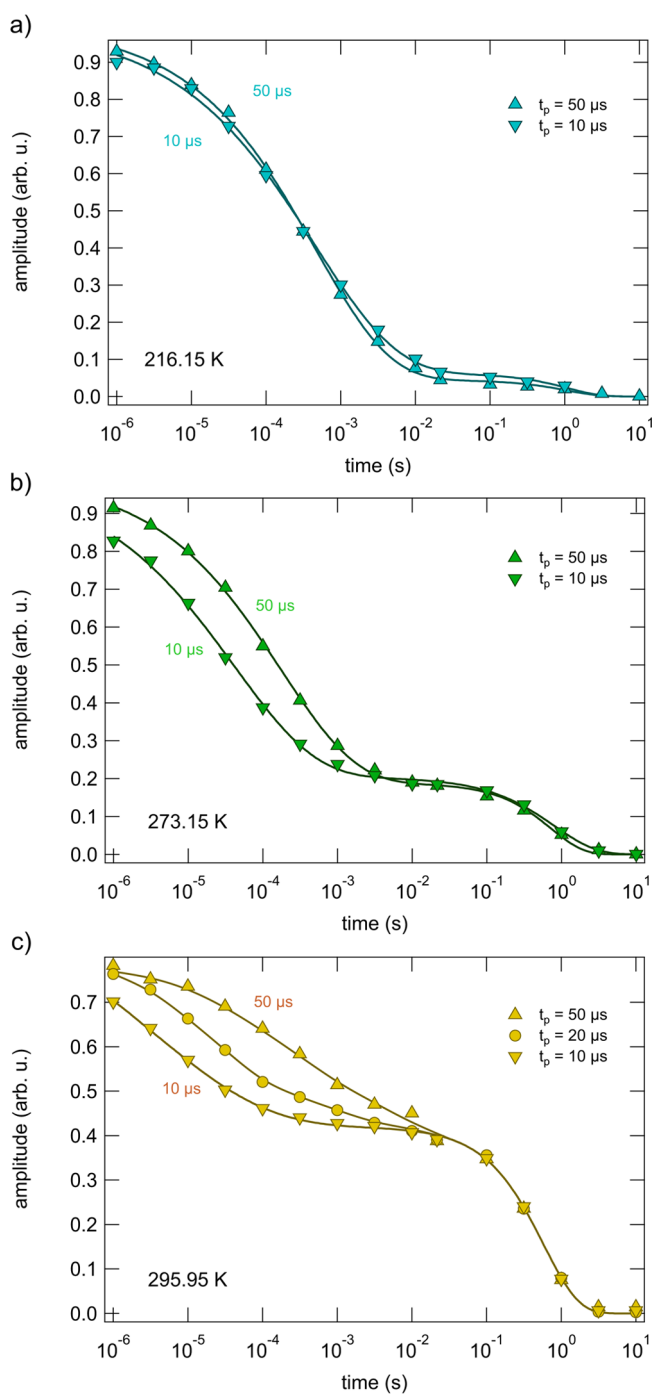


**Figure 7.**  $^7\text{Li}$  SAE NMR echo decay curves,  $S_2(t_p, t_m)$  vs  $t_m$ , that have been recorded at preparation times  $t_p$  equal to or larger than 10  $\mu\text{s}$  but shorter than 50  $\mu\text{s}$ . With increasing  $t_p$ , the first decay step shifts toward larger mixing times  $t_m$ . This is because of motional phase averaging that takes place during the evolution period  $t_p$ . The higher  $T$  is, the more pronounced the effect because Li diffusivity steadily increases with  $T$ .

$t_p$  is, however, apparent,<sup>42</sup> limiting the detection of all of the  $\text{Li}^+$  jump processes (this is best seen at 295 K and above.) The limitation, on the other hand, can be used to estimate the order of magnitude of  $\tau_{\text{SAE}}^{-1}$ : at ambient temperature, it is definitely on the order of  $10^5 \text{ s}^{-1}$ . This is in perfect agreement with the result derived from spin-lock SLR NMR. In particular, it is in perfect agreement with the jump rate ( $4.2 \times 10^5 \text{ s}^{-1}$ ) estimated from



the second SLR NMR rate peak showing up at 313 K (see above).

Knowing about the  $t_p$  dependence on  $S_2'(t_m)$ , we can analyze the associated final state amplitudes. At sufficiently large preparation times, the complete SAE NMR curves are measurable, i.e., proper normalization is possible. In Figure 8,

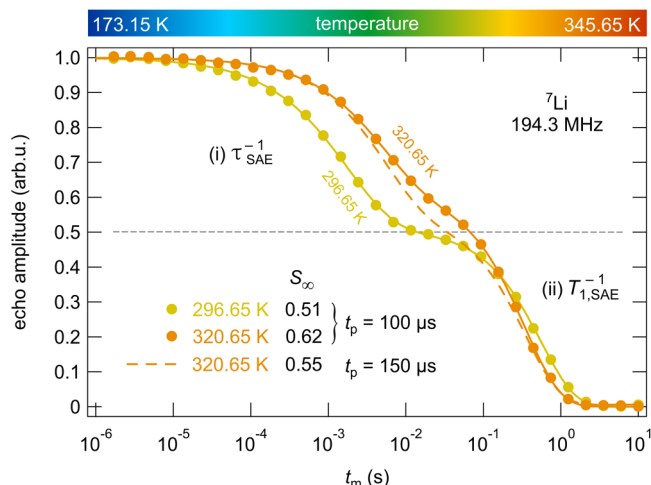


**Figure 8.**  $^7\text{Li}$  SAE NMR decay curves,  $S_2(t_p, t_m)$  vs  $t_m$ , recorded at large preparation times  $t_p$  of up to 150  $\mu\text{s}$ . As is evident from the normalization of  $S_2$  final state amplitudes,  $S_\infty$  between 0.5 and 0.6 show up. The slight increase of  $T_{1,\text{SAE}}$  reflects the temperature dependence of  $T_1$ . The data points refer to the amplitude of the quadrupolar spin-alignment echo. Note that at such large preparation times the whole echo is composed of both a quadrupolar and a dipolar part. The dipolar part, however, behaves very similar compared to the sharp alignment echo. Note that the slight temperature dependence of the second decay step reflects the diffusion-induced increase of  $R_1$  with  $T$  (see Figure 3).

results are shown for 296.65 and 320.65 K; at these temperatures, dipole–dipole interactions, which may affect  $S_\infty$ ,<sup>41</sup> are largely eliminated through rapid  $\text{Li}^+$  exchange; increasing  $T$  further has no effect on the curves.

The corresponding final state amplitudes  $S_\infty$  range from 0.5 to 0.6. Taking into account the site occupancy as derived from neutron diffraction (0.50 (24d), 0.36 (96h), see Table S1),  $S_\infty$  is expected to take a value of 0.62 if we assume this two-site jump process to be mainly responsible for SAE decay. This good agreement with experiment (Figure 8) points to the involvement of the two electrically inequivalent sites in LLZMO. Moreover, the pronounced phase averaging during

$t_p$  indicates that the quadrupole frequencies associated with the sites 24d and 96h are quite different. In such a case, a small number of jumps suffices to cause averaging. Because of dipolar couplings (to some extent, the amplitude  $S_\infty$  depends on  $T$ ),<sup>41</sup> only at sufficiently high  $T$  are these couplings fully averaged.

As a last remark: of course, at temperatures equal to or higher than 270 K, the condition  $t_p \ll \tau_{\text{SAE}}$  is violated. Thus, the influence of phase averaging, which predominantly affects the fraction of species moving fast on the scale set by the evolution time, cannot be neglected, as is shown in Figure 7. Thus, there might be a fast spin reservoir because of heterogeneous dynamics rather than uniform  $\text{Li}^+$  exchange that leads to  $\bar{\omega}_Q(t_m) = \text{const.}$  giving rise to the second decay step seen.

**3.4. Possible Li Ion Diffusion Pathways and Comparison of NMR Activation Energies with Findings from Theory.** In order to ascribe the activation energies found to possible (microscopic)  $\text{Li}^+$  diffusion pathways or elementary jump processes, we first have to look at the crystal structure of LLZMO. The crystal structure ( $Ia\bar{3}d$ ) and, most importantly, the Li site occupancies of our sample have been revealed by neutron diffraction. According to the refinement of neutron powder diffraction data, Mo and Zr ions are distributed over the 16a sites, and La ions occupy the dodecahedra (24c). As mentioned above, according to the best refinement, Li ions reside on two sites, viz., 24d positions with 4-fold coordination (site occupancy 0.5) and 96h sites with distorted 4-fold coordination (site occupancy 0.36). The occupancy of these two sites is in agreement with that found for other LLZO-type garnets.<sup>71</sup> Possible  $\text{Li}^+$  diffusion pathways, simply connecting sites 24d and 96h,<sup>70,71</sup> are shown in Table 1.

The distribution of vacancies, ordered or disordered over the  $\text{Li}^+$  sites,<sup>72,73</sup> as well as repulsive  $\text{Li}^+ - \text{Li}^+$  Coulomb interactions (note that each occupied 24d site (see Figure 9) blocks the occupation of next-neighbored 96h sites)<sup>74</sup> are expected to vary with the synthesis conditions.<sup>75</sup> Annealing temperatures and cooling rates may critically influence lithium ordering<sup>75</sup> and, thus, ionic conductivity that is assumed to depend on total  $\text{Li}^+$  concentration rather than on the kind of doping ions present.<sup>19</sup> In particular, the thermal history of the samples may also cause nonequilibrium  $\text{Li}^+$  distributions over the available voids in garnet-type cubic LLZO that crucially influences its ion transport properties.<sup>75</sup> Thus, coming from real systems, the comparison with results from calculations is by far not straightforward. We should also keep in mind that diffusion pathways chosen by the ions may change with increasing temperature, as has been pointed out by Lai and co-workers for  $\text{Li}_5\text{La}_3\text{Ta}_2\text{O}_{12}$  using classical molecular dynamics simulations.<sup>76</sup>

**Table 1.** Possible Elementary Steps of Li Ion Hopping in LLZMO between Next Neighbors and Tentative Assignment of Activation Energies

sites	$a$ (Å)	$E_a$ (eV)	method	type/comment
96h–48g–96h <sup>a</sup>	0.7	<0.1	$T_1$ (low- $T$ )	“caged dynamics” <sup>b</sup>
24d–96h <sup>c</sup>	1.66	0.15	$T_1$	forward, backward jumps <sup>d</sup>
96h–24d(–96h’)	1.66	0.15	$T_1$	also detectable by SAE NMR (0.29 eV)
24d–[96h]–24d <sup>e</sup>	2.34, 3.12	0.27–0.29	$T_{1e}; \tau_{\text{SAE}}$	
96h–96h <sup>f</sup>	2.47, 2.9, 3.1, 3.47	$\geq 0.29$	$T_{1e}; (\tau_{\text{SAE}})$	including paths bypassing the 24d site; curved pathway

<sup>a</sup>Very fast jump process between similar sites most likely invisible for SAE NMR even at extremely low  $T$ . <sup>b</sup>Strictly localized motions of split site 48g. Only one of the three sites within the pocket can be occupied by Li.  $E_a$  is expected to be extremely small. Note that this movement has not been detected by NMR so far. <sup>c</sup>Fast jump process between similar sites most likely invisible for SAE NMR. <sup>d</sup>Localized two-site jump process. <sup>e</sup>Here, [96h] denotes the split-atom site 96h–48g–96h’; see the first line in the table. <sup>f</sup>Presumably, this process, which bypasses the 24d site, involves temporary occupation of voids connecting the two 96h sites; it is most likely also visible by SAE NMR at low temperatures.

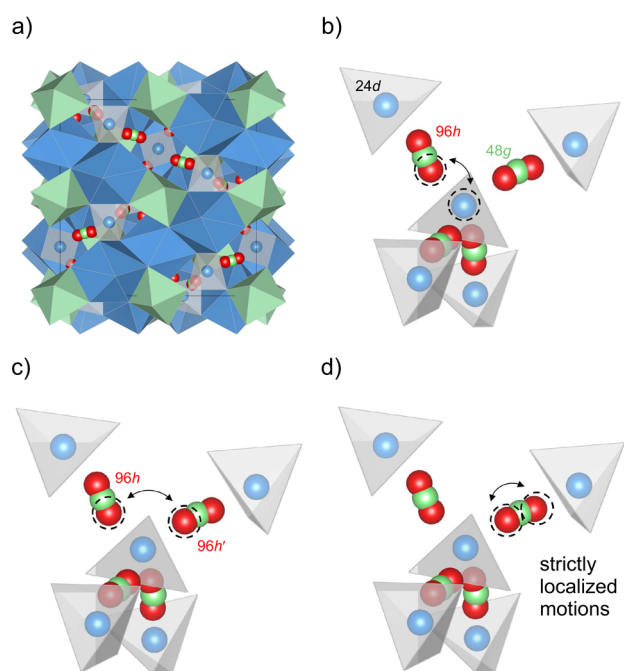


**Figure 9.** (a) Crystal structure of cubic LLZO (view along the *a*-axis); (b–d) selected Li elementary hopping steps between sites 24d and 96h that are occupied by Li in LLZMO, as evidenced from neutron diffraction. In (b), the 24d–96h jump process is shown; in (c), Li<sup>+</sup> diffusion between 96h sites of two different octahedral voids is illustrated. (d) Strictly localized Li motions within the 96h–48g–96h' arrangement.

Recent theoretical investigations on overall ion conductivity, diffusion pathways, and local hopping barriers reflect a highly complex picture of ion transport through LLZO. Long-range ion transport in cubic LLZO, to which (dc)-conductivity measurements are sensitive, is reported to be governed by an average activation energy of ca. 0.32 to 0.34 eV. The final result of Adams and co-workers (0.34 eV),<sup>74</sup> who studied the 3D network pathway consisting of connected local 24d–96h–24d paths (see Table 1 and Figure 9), agrees well with the study performed by Jalem et al.<sup>77</sup> that reported on a concerted diffusion mechanism (0.33 eV); both groups used molecular dynamics simulations to describe Li<sup>+</sup> motions in the stabilized cubic polymorph at high temperatures. For Ta-bearing LLZO, Ceder and co-workers reported an activation energy of 0.19 eV by considering the 96h–24d(–96h') pathway; this value points to the activation energy we observed via *T*<sub>1</sub> SLR NMR that is sensing short-range ion dynamics.<sup>78</sup>

Two further studies have been published that focus on the elementary steps of ion hopping in LLZO-type garnets. The *ab initio* calculations based on density functional theory performed by Xu et al.<sup>70</sup> differentiate between two possible Li-ion hopping pathways. The first route describes Li-ion hopping between (96h/48g) and (96h/48g)' voids in garnets (Figure 9c); this pathway is characterized by a rather large hopping barrier. According to the second route,<sup>70</sup> the Li ion moves through the (96h/48g)–24d border (Figure 9c), thus crossing the shared triangular face (0.25 eV). Then, the ion shortly stays at the corner of the 24d site before climbing over the other barrier and finally reaching the empty 24d site (cf. also the considerations of Awaka et al.<sup>71</sup>). This (edge pass-type) pathway would be consistent with that roughly denoted 96h–24d(–96h') in Table 1. The overall barrier reported by Xu et

al.<sup>70</sup> is 0.26 eV, which is in excellent agreement to that seen via NMR relaxometry on our sample; see above. As suggested by Lai et al.,<sup>76</sup> in Li<sub>5</sub>La<sub>3</sub>Ta<sub>2</sub>O<sub>12</sub> there might be a change from this edge-passing mechanism at low temperatures to a center-passing one at higher *T*. In the case of Li<sub>5</sub>La<sub>3</sub>Ta<sub>2</sub>O<sub>12</sub>, the authors, who used reverse Monte Carlo modeling and classical molecular dynamics to understand local lithium structure and dynamics, do not find any evidence for direct jumps between the octahedral voids, i.e., bypassing the 24d bottleneck.<sup>76</sup> The latter has also been observed by Miara et al.<sup>78</sup>

Coming back to our results from NMR relaxometry, we indeed observe two different relaxation rate peaks (*R*<sub>1*ρ*</sub>). This points to two types of Li-ion motional processes in our sample. Tentatively, we would assign the rate peak showing up at lower *T* to Li motions between 24d and 96h sites (Figure 9b). The corresponding sites are separated by ca. 1.66 Å; because of Coulomb repulsion, it is expected that they cannot be occupied simultaneously. Likely, this hopping process also influences the *R*<sub>1</sub> rates (0.15 eV). From our measurements, we find no indications that the Li ions on 24d sites do not participate in Li<sup>+</sup> diffusion, as assumed for, e.g., Li<sub>5</sub>La<sub>3</sub>Nb<sub>2</sub>O<sub>12</sub> on the basis of <sup>6</sup>Li 2D exchange NMR.<sup>79</sup> For comparison with theory, it is common in theoretical investigations to observe that 24d sites do indeed participate in Li<sup>+</sup> diffusion (see above). The second NMR relaxation rate peak observed via *R*<sub>1*ρ*</sub> might be attributed to Li-ion hopping between 96h sites either temporarily occupying or even bypassing the 24d sites (see Table 1). As pointed out by Meier et al.,<sup>80</sup> short-distance jumps between face-sharing tetrahedra (24d) and octahedra (96h/48g) exhibit a slightly smaller energetic barrier than jumps between the neighboring, edge-sharing polyhedra (96h).

In detail, Meier et al. used *ab initio* molecular dynamics simulation, metadynamics, and nudged-elastic band calculations to systematically describe Li-ion hopping in cubic and tetragonal LLZO.<sup>80</sup> While for the tetragonal modification the motion of Li ions is reported to be influenced by collective nature, they identified an asynchronous mechanism dominated by single-ion jumps and induced collective motion for cubic LLZO. On the assumption of individual jumps, the activation energies for a series of elementary hopping processes along the Li<sup>+</sup> diffusion path in LLZO, involving the 24d and (96h/48g) sites, in particular, are on the order of ca. 0.10 to 0.30 eV.<sup>80</sup> The activation energies of our NMR measurements perfectly agree with this range. For comparison, these barriers are significantly lower than the mean activation energy for Li-ion hopping in the tetragonal modification (0.4 eV), for which 0.32 eV ( $\omega_1\tau_c \gg 1$ ) and 0.48 eV ( $\omega_1\tau_c \ll 1$ ) was recently found using spin-lock NMR relaxometry (as mentioned above).<sup>31</sup>

As a last remark, the Li ions in the (96h/48g) void, i.e., the split site 96h–48g–96h', which can be occupied only by a single Li ion, might give rise to strictly localized Li<sup>+</sup> displacements (Figure 9d). Such caged dynamics would give rise to a phenomenon that is frequently related to a nearly constant loss, that is, a frequency-independent  $\epsilon''$  being the imaginary part of the complex permittivity. This translates into a temperature-independent conductivity that linearly increases with frequency at sufficiently low *T*. For such motions, activation energies below 0.1 eV are reasonable. Further studies are needed to clarify whether this phenomenon can indeed be detected in LLZO-type garnets.

## 4. CONCLUSIONS

$\text{Li}_{6.5}\text{La}_3\text{Zr}_{1.75}\text{Mo}_{0.25}\text{O}_{12}$  represents a new, fast lithium-ion conductor that crystallizes with cubic symmetry. The fact that it is stabilized in its cubic modification without doping with trivalent cations such as Al or Ga, leaves the Li sublattice untouched by any dopants that could possibly disturb the 3D network pathway used by Li ions for long-range diffusion.

We used various  $^7\text{Li}$  solid-state NMR spectroscopic tools to analyze Li-ion dynamics on both the short- and long-range length scales. It is difficult to obtain such information from impedance spectroscopy that is usually applied to characterize ion transport in LLZO-based materials. Li diffusivity in LLZMO turns out to be remarkably high but has to be described by multiple Li-ion dynamic processes taking place. Depending on the time window to which the different NMR methods are sensitive, (mean) activation energies were extracted that range from 0.15 eV ( $R_1$ ) to 0.29 eV ( $R_{1Q}$ , SAE NMR).

In particular, the two-step damping of variable-temperature sin–sin correlation functions of SAE NMR reveals heterogeneous dynamics. The applicability of SAE NMR, which is sensitive to ion hopping between electrically inequivalent sites in LLZO, shows that both 24d and 96h sites are involved in  $\text{Li}^+$  diffusion. This is underlined by the two-step behavior observed. Echo damping at large preparation times might be adduced to find indications that a two-site jump process, 96h–24d–96h', is present in LLZMO. At least for LLZMO, this rules out previous considerations about immobile Li ions residing on 24d.

The behavior of the  $R_{1Q}$  rates with temperature can be approximated at best with two BPP fits. The peak at 313 K points to an  $\text{Li}^+$  jump rate of  $4.2 \times 10^5 \text{ s}^{-1}$ . This value is in perfect agreement with the jump rate expected from SAE NMR if we extrapolate the  $\tau_{\text{SAE}}^{-1}$  rates toward higher  $T$ . The rate transforms into a self-diffusion coefficient  $D$  of ca.  $1.9 \times 10^{-11} \text{ cm}^2 \text{ s}^{-1}$ . Interestingly, the diffusion-induced rate peaks  $R_{1Q}(1/T)$  observed appear to be sharper than has been observed for Al-doped LLZO, indicating a less broad distribution of jump rates for LLZMO with a dopant-free Li sublattice. Extremely broad  $R_{1Q}(1/T)$  peaks seem to be characteristic merely for Al- or Ga-stabilized LLZO. The activation energies found have tentatively been assigned to possible elementary Li-ion hopping processes between neighboring  $\text{Li}^+$  sites 24d and 96h. Remarkably, our results agree very well with local hopping barriers that have been calculated on the basis of density functional theory.

## ■ ASSOCIATED CONTENT

### Supporting Information

The Supporting Information is available free of charge on the ACS Publications website at DOI: [10.1021/acs.chemmater.5b02231](https://doi.org/10.1021/acs.chemmater.5b02231).

Results from neutron diffraction experiments including the site occupancies found (PDF).

## ■ AUTHOR INFORMATION

### Corresponding Authors

\*(P.B.) E-mail: [bottke@tugraz.at](mailto:bottke@tugraz.at).

\*(M.W.) E-mail: [wilkening@tugraz.at](mailto:wilkening@tugraz.at).

### Notes

The authors declare no competing financial interest.

## ■ ACKNOWLEDGMENTS

We thank our colleagues at the TU Graz for valuable discussions. Financial support by the Deutsche Forschungsgemeinschaft (DFG Research Unit 1277, grant nos. WI3600/2-2 and 4-1) as well as by the Austrian Federal Ministry of Science, Research and Economy, and the Austrian National Foundation for Research, Technology and Development is greatly appreciated. Moreover, we thank the Austrian Science Fund (FWF), project no. P25702 (D. Rettenwander, G. Amthauer), for financial support.

## ■ REFERENCES

- (1) Larcher, D.; Tarascon, J.-M. Towards Greener and More Sustainable Batteries for Electrical Energy Storage. *Nat. Chem.* **2015**, *7*, 19–29.
- (2) Adelhelm, P.; Hartmann, P.; Bender, C. L.; Busche, M.; Eufinger, C.; Janek, J. From Lithium to Sodium: Cell Chemistry of Room Temperature Sodium-Air and Sodium-Sulfur Batteries. *Beilstein J. Nanotechnol.* **2015**, *6*, 1016–1055.
- (3) Bruce, P. G.; Freunberger, S. A.; Hardwick, L. J.; Tarascon, J.-M. Li-O<sub>2</sub> and Li-S Batteries with High Energy Storage. *Nat. Mater.* **2012**, *11*, 19–29.
- (4) Aricó, A. S.; Bruce, P.; Scrosati, B.; Tarascon, J.-M.; van Schalkwijk, W. Nanostructured Materials for Advanced Energy Conversion and Storage Devices. *Nat. Mater.* **2005**, *4*, 366–377.
- (5) Whittingham, M. S. Lithium Batteries and Cathode Materials. *Chem. Rev.* **2004**, *104*, 4271–4301.
- (6) Knauth, P. Inorganic Solid Li Ion Conductors: An Overview. *Solid State Ionics* **2009**, *180*, 911–916.
- (7) Cao, C.; Li, Z.; Wang, X.-L.; Zhao, X.; Han, W.-Q. Recent Advances in Inorganic Solid Electrolytes for Lithium Batteries. *Front. Energy Res.* **2014**, *2*, 25.
- (8) Jung, Y. S.; Oh, D. Y.; Nam, Y. J.; Park, K. H. Issues and Challenges for Bulk-Type All-Solid-State Rechargeable Lithium Batteries using Sulfide Solid Electrolytes. *Isr. J. Chem.* **2015**, *55*, 472–485.
- (9) Murugan, R.; Thangadurai, V.; Weppner, W. Fast Lithium Ion Conduction in Garnet-Type  $\text{Li}_7\text{La}_3\text{Zr}_2\text{O}_{12}$ . *Angew. Chem., Int. Ed.* **2007**, *46*, 7778–7781.
- (10) Kamaya, N.; Homma, K.; Yamakawa, Y.; Hirayama, M.; Kanno, R.; Yonemura, M.; Kamiyama, T.; Kato, Y.; Hama, S.; Kawamoto, K.; Mitsui, A. A Lithium Superionic Conductor. *Nat. Mater.* **2011**, *10*, 682–686.
- (11) Mizuno, F.; Hayashi, A.; Tadanaga, K.; Tatsumisago, M. New, Highly Ion-Conductive Crystals Precipitated from  $\text{Li}_2\text{S-P}_2\text{S}_5$  Glasses. *Adv. Mater.* **2005**, *17*, 918–921.
- (12) Deiseroth, H.-J.; Kong, S.-T.; Eckert, H.; Vannahme, J.; Reiner, C.; Zaiß, T.; Schlosser, M.  $\text{Li}_6\text{PS}_5\text{X}$ : A Class of Crystalline Li-Rich Solids With an Unusually High  $\text{Li}^+$  Mobility. *Angew. Chem., Int. Ed.* **2008**, *47*, 755–758.
- (13) Epp, V.; Gün, O.; Deiseroth, H.-J.; Wilkening, M. Highly Mobile Ions: Low Temperature NMR Directly Probes Extremely Fast  $\text{Li}^+$  Hopping in Argyrodite-Type  $\text{Li}_6\text{PSe}_3\text{Br}$ . *J. Phys. Chem. Lett.* **2013**, *4*, 2118–2123.
- (14) Kaib, T.; Haddadpour, S.; Kapitein, M.; Bron, P.; Schröder, C.; Eckert, H.; Roling, B.; Dehnen, S. New Lithium Chalcogenidotetrelates,  $\text{LiChT}$ : Synthesis and Characterization of the  $\text{Li}^+$ -Conducting Tetralithium ortho-Sulfidostannate  $\text{Li}_4\text{SnS}_4$ . *Chem. Mater.* **2012**, *24*, 2211–2219.
- (15) Bron, P.; Johansson, S.; Zick, K.; Schmedt auf der Günne, J.; Dehnen, S.; Roling, B.  $\text{Li}_{10}\text{SnP}_2\text{S}_{12}$ : An Affordable Lithium Superionic Conductor. *J. Am. Chem. Soc.* **2013**, *135*, 15694–15697.
- (16) Sahu, G.; Lin, Z.; Li, J.; Liu, Z.; Dudney, N.; Liang, C. Air-Stable, High-Conduction Solid Electrolytes of Arsenic-Substituted  $\text{Li}_4\text{SnS}_4$ . *Energy Environ. Sci.* **2014**, *7*, 1053–1058.
- (17) López, M. C.; Ortiz, G. F.; Arroyo-de Dompablo, E. M.; Tirado, J. L. An Unnoticed Inorganic Solid Electrolyte: Dilithium Sodium



Phosphate with the Nalipoite Structure. *Inorg. Chem.* **2014**, *53*, 2310–2316.

(18) Brant, J. A.; Massi, D. M.; Holzwarth, N. A. W.; MacNeil, J. H.; Douvalis, A. P.; Bakas, T.; Martin, S. W.; Gross, M. D.; Aitken, J. A. Fast Lithium Ion Conduction in  $\text{Li}_2\text{SnS}_3$ : Synthesis, Physicochemical Characterization, and Electronic Structure. *Chem. Mater.* **2015**, *27*, 189–196.

(19) Thangadurai, V.; Narayanan, S.; Pinzaru, D. Garnet-Type Solid-State Fast Li Ion Conductors for Li Batteries: A Critical Review. *Chem. Soc. Rev.* **2014**, *43*, 4714–4727.

(20) Wolfenstine, J.; Allen, J. L.; Read, J.; Sakamoto, J. Chemical Stability of Cubic  $\text{Li}_7\text{La}_3\text{Zr}_2\text{O}_{12}$  with Molten Lithium at Elevated Temperature. *J. Mater. Sci.* **2013**, *48*, 5846–5851.

(21) Buschmann, H.; Dölle, J.; Berendts, S.; Kuhn, A.; Bottke, P.; Wilkening, M.; Heitjans, P.; Senyshyn, A.; Ehrenberg, H.; Lotnyk, A.; Duppel, V.; Kienle, L.; Janek, J. Structure and Dynamics of the Fast Lithium Ion Conductor “ $\text{Li}_7\text{La}_3\text{Zr}_2\text{O}_{12}$ ”. *Phys. Chem. Chem. Phys.* **2011**, *13*, 19378–19392.

(22) Rettenwander, D.; Geiger, C. A.; Tribus, M.; Tropper, P.; Amthauer, G. A Synthesis and Crystal Chemical Study of the Fast Ion Conductor  $\text{Li}_{7-3x}\text{Ga}_x\text{La}_3\text{Zr}_2\text{O}_{12}$  with  $x = 0.08$  to  $0.84$ . *Inorg. Chem.* **2014**, *53*, 6264–6269.

(23) Wolfenstine, J.; Ratchford, J.; Rangasamy, E.; Sakamoto, J.; Allen, J. L. Synthesis and High Li-Ion Conductivity of Ga-Stabilized Cubic  $\text{Li}_7\text{La}_3\text{Zr}_2\text{O}_{12}$ . *Mater. Chem. Phys.* **2012**, *134*, 571–575.

(24) Allen, J. L.; Wolfenstine, J.; Rangasamy, E.; Sakamoto, J. Effect of Substitution (Ta, Al, Ga) on the Conductivity of  $\text{Li}_7\text{La}_3\text{Zr}_2\text{O}_{12}$ . *J. Power Sources* **2012**, *206*, 315–319.

(25) Jalem, R.; Rushton, M.; Manalastas, W.; Nakayama, M.; Kasuga, T.; Kilner, J. A.; Grimes, R. W. Effects of Gallium Doping in Garnet-Type  $\text{Li}_7\text{La}_3\text{Zr}_2\text{O}_{12}$  Solid Electrolytes. *Chem. Mater.* **2015**, *27*, 2821–2831.

(26) Rettenwander, D.; Geiger, C. A.; Amthauer, G. Synthesis and Crystal Chemistry of the Fast Li-Ion Conductor  $\text{Li}_7\text{La}_3\text{Zr}_2\text{O}_{12}$  Doped with Fe. *Inorg. Chem.* **2013**, *52*, 8005–8009.

(27) Bernstein, N.; Johannes, M. D.; Hoang, K. Origin of the Structural Phase Transition in  $\text{Li}_7\text{La}_3\text{Zr}_2\text{O}_{12}$ . *Phys. Rev. Lett.* **2012**, *109*, 205702.

(28) Rangasamy, E.; Wolfenstine, J.; Sakamoto, J. The Role of Al and Li Concentration on the Formation of Cubic Garnet Solid Electrolyte of Nominal Composition  $\text{Li}_7\text{La}_3\text{Zr}_2\text{O}_{12}$ . *Solid State Ionics* **2012**, *206*, 28–32.

(29) Awaka, J.; Kijima, N.; Hayakawa, H.; Akimoto, J. Synthesis and Structure Analysis of Tetragonal  $\text{Li}_7\text{La}_3\text{Zr}_2\text{O}_{12}$  with the Garnet-Related Type Structure. *J. Solid State Chem.* **2009**, *182*, 2046–2052.

(30) Ramakumar, S.; Satyanarayana, L.; Manorama, S. V.; Murugan, R. Structure and  $\text{Li}^+$  Dynamics of Sb-Doped  $\text{Li}_7\text{La}_3\text{Zr}_2\text{O}_{12}$  Fast Lithium Ion Conductors. *Phys. Chem. Chem. Phys.* **2013**, *15*, 11327–11338.

(31) Kuhn, A.; Narayanan, S.; Spencer, L.; Goward, G.; Thangadurai, V.; Wilkening, M. Li Self-Diffusion in Garnet-type  $\text{Li}_7\text{La}_3\text{Zr}_2\text{O}_{12}$  as Probed Directly by Diffusion-Induced  $^7\text{Li}$  Spin-Lattice Relaxation NMR Spectroscopy. *Phys. Rev. B: Condens. Matter Mater. Phys.* **2011**, *83*, 094302.

(32) Kuhn, A.; Epp, V.; Schmidt, G.; Narayanan, S.; Thangadurai, V.; Wilkening, M. Spin-Alignment Echo NMR: Probing  $\text{Li}^+$  Hopping Motion in the Solid Electrolyte  $\text{Li}_7\text{La}_3\text{Zr}_2\text{O}_{12}$  with Garnet-Type Tetragonal Structure. *J. Phys.: Condens. Matter* **2012**, *24*, 035901.

(33) Tang, X.-P.; Wu, Y. Alignment Echo of Spin-3/2  $^9\text{Be}$  Nuclei: Detection of Ultraslow Motion. *J. Magn. Reson.* **1998**, *133*, 155–165.

(34) Tang, X.-P.; Busch, R.; Johnson, W.; Wu, Y. Slow Atomic Motion in Zr-Ti-Cu-Ni-Be Metallic Glasses Studied by NMR. *Phys. Rev. Lett.* **1998**, *81*, 5358–5361.

(35) Tang, X.-P.; Geyer, U.; Busch, R.; Johnson, W.; Wu, Y. Diffusion Mechanisms in Metallic Supercooled Liquids and Glasses. *Nature* **1999**, *402*, 160–162.

(36) Böhmer, R.; Jörg, T.; Qi, F.; Titze, A. Stimulated Echo NMR Spectroscopy of Slow Ionic Motions in a Solid Electrolyte. *Chem. Phys. Lett.* **2000**, *316*, 419–424.

(37) Qi, F.; Jörg, T.; Böhmer, R. Stimulated-Echo NMR Spectroscopy of  $^9\text{Be}$  and  $^7\text{Li}$  in Solids: Method and Application to Ion Conductors. *Solid State Nucl. Magn. Reson.* **2002**, *22*, 484–500.

(38) Böhmer, R.; Jeffrey, K.; Vogel, M. Solid-state Lithium NMR with Applications to the Translational Dynamics in Ion Conductors. *Prog. Nucl. Magn. Reson. Spectrosc.* **2007**, *50*, 87–174.

(39) Wilkening, M.; Heitjans, P. From Micro to Macro: Access to Long-Range  $\text{Li}^+$  Diffusion Parameters in Solids via Microscopic  $^6\text{Li}/^7\text{Li}$  Spin-Alignment Echo NMR Spectroscopy. *ChemPhysChem* **2012**, *13*, 53–65.

(40) Wilkening, M.; Küchler, W.; Heitjans, P. From Ultraslow to Fast Lithium Diffusion in the 2D Ion Conductor  $\text{Li}_{0.7}\text{TiS}_2$  Probed Directly by Stimulated-Echo NMR and Nuclear Magnetic Relaxation. *Phys. Rev. Lett.* **2006**, *97*, 065901.

(41) Qi, F.; Diezemann, G.; Böhm, H.; Lambert, J.; Böhmer, R. Simple Modeling of Dipolar Coupled  $^7\text{Li}$  Spins and Stimulated-Echo Spectroscopy of Single-Crystalline  $\beta$ -Eucryptite. *J. Magn. Reson.* **2004**, *169*, 225–239.

(42) Qi, F.; Rier, C.; Böhmer, R.; Franke, W.; Heitjans, P. Ion Hopping in Crystalline and Glassy Spodumene  $\text{LiAlSi}_2\text{O}_6$ : Spin-Lattice Relaxation and  $^7\text{Li}$  Echo NMR Spectroscopy. *Phys. Rev. B: Condens. Matter Mater. Phys.* **2005**, *72*, 104301.

(43) Wilkening, M.; Heine, J.; Lyness, C.; Armstrong, A. R.; Bruce, P. G. Li Diffusion Properties of Mixed Conducting  $\text{TiO}_2$ -B Nanowires. *Phys. Rev. B: Condens. Matter Mater. Phys.* **2009**, *80*, 064302.

(44) Wilkening, M.; Gebauer, D.; Heitjans, P. Diffusion Parameters in Single-Crystalline  $\text{Li}_3\text{N}$  as Probed by  $^6\text{Li}$  and  $^7\text{Li}$  Spin-Alignment Echo NMR Spectroscopy in Comparison with Results from  $^8\text{Li}$   $\beta$ -Radiation Detected NMR. *J. Phys.: Condens. Matter* **2008**, *20*, 022201.

(45) Wilkening, M.; Mühle, C.; Jansen, M.; Heitjans, P. Microscopic Access to Long-Range Diffusion Parameters of the Fast Lithium Ion Conductor  $\text{Li}_7\text{BiO}_6$  by Solid State  $^7\text{Li}$  Stimulated Echo NMR. *J. Phys. Chem. B* **2007**, *111*, 8691–8694.

(46) Faske, S.; Koch, B.; Murawski, S.; Küchler, R.; Böhmer, R.; Melchior, J.; Vogel, M. Mixed-Cation  $\text{Li}_x\text{Ag}_{1-x}\text{PO}_3$  Glasses Studied by  $^6\text{Li}$ ,  $^7\text{Li}$ , and  $^{109}\text{Ag}$  Stimulated-Echo NMR Spectroscopy. *Phys. Rev. B: Condens. Matter Mater. Phys.* **2011**, *84*, 024202.

(47) Brinkmann, C.; Faske, S.; Koch, B.; Vogel, M. NMR Multi-Time Correlation Functions of Ion Dynamics in Solids. *Z. Phys. Chem.* **2010**, *224*, 1535–1553.

(48) Böhmer, R.; Qi, F. Spin Relaxation and Ultra-Slow Li Transport in an Aluminosilicate Glass Ceramic. *Solid State Nucl. Magn. Reson.* **2007**, *31*, 28–34.

(49) Wagner, R.; Rettenwander, D.; Welzl, A.; Schmidt, W.; Fleig, J.; Wilkening, M.; Amthauer, G. A comparative study of the synthesis of coarse-grained  $\text{Li}_{6.4}\text{M}_{0.2}\text{La}_3\text{Zr}_2\text{O}_{12}$  with  $\text{M} = \text{Al}, \text{Ga}, \text{or Fe}$ , to be published.

(50) Fukushima, E.; Roeder, S. *Experimental Pulse NMR*; Addison-Wesley: Reading, MA, 1981.

(51) Heitjans, P.; Schirmer, A.; Indris, S. In *Diffusion in Condensed Matter: Methods, Materials Models*, 2nd ed.; Heitjans, P., Kärger, J., Eds.; Springer, Berlin, 2005; Chapter 9, pp 369–415.

(52) Ailion, D.; Slichter, C. P. Study of Ultraslow Atomic Motions by Magnetic Resonance. *Phys. Rev. Lett.* **1964**, *12*, 168–171.

(53) Ailion, D. C.; Slichter, C. P. Observation of Ultra-Slow Translational Diffusion in Metallic Lithium by Magnetic Resonance. *Phys. Rev.* **1965**, *137*, A235–A245.

(54) Slichter, C. P.; Ailion, D. Low-Field Relaxation and the Study of Ultraslow Atomic Motions by Magnetic Resonance. *Phys. Rev.* **1964**, *135*, A1099–A1110.

(55) Epp, V.; Gün, O.; Deiseroth, H.-J.; Wilkening, M. Long-Range Li Dynamics in the Lithium Argyrodite  $\text{Li}_7\text{PSe}_6$  as Probed by Rotating-Frame Spin-Lattice Relaxation NMR. *Phys. Chem. Chem. Phys.* **2013**, *15*, 7123–7132.

(56) Stanje, B.; Epp, V.; Nakhal, S.; Lerch, M.; Wilkening, M. Li Ion Dynamics along the Inner Surfaces of Layer-Structured  $2\text{H-Li}_x\text{NbS}_2$ . *ACS Appl. Mater. Interfaces* **2015**, *7*, 4089–4099.

(57) Dunst, A.; Epp, V.; Hanzu, I.; Freunberger, S. A.; Wilkening, M. Short-Range Li Diffusion vs. Long-Range Ionic Conduction in



Nanocrystalline Lithium Peroxide  $\text{Li}_2\text{O}_2$  - the Discharge Product in Lithium-Air Batteries. *Energy Environ. Sci.* **2014**, 7, 2739–2752.

(58) Langer, J.; Epp, V.; Heitjans, P.; Mautner, F. A.; Wilkening, M. Li Motion in the Anode Material  $\text{LiC}_6$  as Seen via Time-domain  $^7\text{Li}$  NMR. *Phys. Rev. B: Condens. Matter Mater. Phys.* **2013**, 88, 094304.

(59) Jeener, J.; Broekaert, P. Nuclear Magnetic Resonance in Solids: Thermodynamic Effects of a Pair of rf Pulses. *Phys. Rev.* **1967**, 157, 232–240.

(60) Abragam, A. *The Principles of Nuclear Magnetism*; Clarendon: Oxford, 1961.

(61) Wilkening, M.; Epp, V.; Feldhoff, A.; Heitjans, P. Tuning the Li Diffusivity of Poor Ionic Conductors by Mechanical Treatment: High Li Conductivity of Strongly Defective  $\text{LiTaO}_3$  Nanoparticles. *J. Phys. Chem. C* **2008**, 112, 9291–9300.

(62) Küchler, W.; Heitjans, P.; Payer, A.; Schöllhorn, R.  $^7\text{Li}$  NMR Relaxation by Diffusion in Hexagonal and Cubic  $\text{Li}_x\text{TiS}_2$ . *Solid State Ionics* **1994**, 70/71, 434–438.

(63) Wilkening, M.; Heitjans, P. Li Jump Process in  $h\text{-Li}_{0.7}\text{TiS}_2$  Studied by Two-Time  $^7\text{Li}$  Spin-Alignment Echo NMR and Comparison with Results on Two-Dimensional Diffusion from Nuclear Magnetic Relaxation. *Phys. Rev. B: Condens. Matter Mater. Phys.* **2008**, 77, 024311.

(64) Bunde, A.; Dieterich, W.; Maass, P.; Meyer, M. In *Diffusion in Condensed Matter: Methods, Materials, Models*, 2nd ed.; Heitjans, P., Kärger, J., Eds.; Springer, Berlin, 2005; Chapter 20, pp 813–856.

(65) Funke, K. Jump Relaxation in Solid Electrolytes. *Prog. Solid State Chem.* **1993**, 22, 111–195.

(66) Meyer, M.; Maass, P.; Bunde, A. Spin Lattice Relaxation: Non-BPP-Behavior by Structural Disorder and Coulomb Interactions. *Phys. Rev. Lett.* **1993**, 71, 573–576.

(67) Tse, D.; Hartmann, S. R. Nuclear Spin-Lattice Relaxation via Paramagnetic Centers without Spin Diffusion. *Phys. Rev. Lett.* **1968**, 21, 511–514.

(68) Ruprecht, B.; Billetter, H.; Ruschewitz, U.; Wilkening, M. Ultra-Slow Li Ion Dynamics in  $\text{Li}_2\text{C}_2$  - On the Similarities of Results from  $^7\text{Li}$  Spin-Alignment Echo NMR and Impedance Spectroscopy. *J. Phys.: Condens. Matter* **2010**, 22, 245901.

(69) Ruprecht, B.; Wilkening, M.; Uecker, R.; Heitjans, P. Extremely Slow Li Ion Dynamics in Monoclinic  $\text{Li}_2\text{TiO}_3$  - Probing Macroscopic Jump Diffusion via  $^7\text{Li}$  NMR Stimulated Echoes. *Phys. Chem. Chem. Phys.* **2012**, 14, 11974–11980.

(70) Xu, M.; Park, M. S.; Lee, J. M.; Kim, T. Y.; Park, Y. S.; Ma, E. Mechanisms of  $\text{Li}^+$  Transport in Garnet-Type Cubic  $\text{Li}_{3+x}\text{La}_3\text{M}_2\text{O}_{12}$  ( $\text{M} = \text{Te}, \text{Nb}, \text{Zr}$ ). *Phys. Rev. B: Condens. Matter Mater. Phys.* **2012**, 85, 052301.

(71) Awaka, J.; Takashima, A.; Kataoka, K.; Kijima, N.; Idemoto, Y.; Akimoto, J. Crystal Structure of Fast Lithium-ion-conducting Cubic  $\text{Li}_7\text{La}_3\text{Zr}_2\text{O}_{12}$ . *Chem. Lett.* **2011**, 40, 60–62.

(72) Cussen, E. J. The structure of lithium garnets: cation disorder and clustering in a new family of fast  $\text{Li}^+$  conductors. *Chem. Commun.* **2006**, 412–413.

(73) Li, Y.; Han, J.-T.; Wang, C.-A.; Vogel, S. C.; Xie, H.; Xu, M.; Goodenough, J. B. Ionic Distribution and Conductivity in Lithium Garnet  $\text{Li}_7\text{La}_3\text{Zr}_2\text{O}_{12}$ . *J. Power Sources* **2012**, 209, 278–281.

(74) Adams, S.; Rao, R. P. Ion Transport and Phase Transition in  $\text{Li}_{7-x}\text{La}_3(\text{Zr}_{2-x}\text{M}_x)\text{O}_{12}$  ( $\text{M} = \text{Ta}^{5+}, \text{Nb}^{5+}$ ,  $x = 0, 0.25$ ). *J. Mater. Chem.* **2012**, 22, 1426–1434.

(75) Rao, R. P.; Gu, W.; Sharma, N.; Peterson, V. K.; Avdeev, M.; Adams, S. In Situ Neutron Diffraction Monitoring of  $\text{Li}_7\text{La}_3\text{Zr}_2\text{O}_{12}$  Formation: Toward a Rational Synthesis of Garnet Solid Electrolytes. *Chem. Mater.* **2015**, 27, 2903–2910.

(76) Wang, Y.; Klenk, M.; Page, K.; Lai, W. Local Structure and Dynamics of Lithium Garnet Ionic Conductors: A Model Material  $\text{Li}_3\text{La}_3\text{Ta}_2\text{O}_{12}$ . *Chem. Mater.* **2014**, 26, 5613–5624.

(77) Jalem, R.; Yamamoto, Y.; Shiiba, H.; Nakayama, M.; Munakata, H.; Kasuga, T.; Kanamura, K. Concerted Migration Mechanism in the Li Ion Dynamics of Garnet-Type  $\text{Li}_7\text{La}_3\text{Zr}_2\text{O}_{12}$ . *Chem. Mater.* **2013**, 25, 425–430.

(78) Miara, L. J.; Ong, S. P.; Mo, Y.; Richards, W. D.; Park, Y.; Lee, J.-M.; Lee, H. S.; Ceder, G. Effect of Rb and Ta Doping on the Ionic Conductivity and Stability of the Garnet  $\text{Li}_{7+2x-y}(\text{La}_{3-x}\text{Rb}_x)(\text{Zr}_{2-y}\text{Ta}_y)\text{O}_{12}$  ( $0 \leq x \leq 0.375$ ,  $0 \leq y \leq 1$ ) Superionic Conductor: A First Principles Investigation. *Chem. Mater.* **2013**, 25, 3048–3055.

(79) van Wüllen, L.; Echelmeyer, T.; Meyer, H.-W.; Wilmer, D. The Mechanism of Li-Ion Transport in the Garnet  $\text{Li}_5\text{La}_3\text{Nb}_2\text{O}_{12}$ . *Phys. Chem. Chem. Phys.* **2007**, 9, 3298–3303.

(80) Meier, K.; Laino, T.; Curioni, A. Solid-State Electrolytes: Revealing the Mechanisms of Li-Ion Conduction in Tetragonal and Cubic LLZO by First-Principles Calculations. *J. Phys. Chem. C* **2014**, 118, 6668–6679.